**Original Research Article**

# New Binary Hausdorff Symmetry measure based seeded region growing for retinal vessel segmentation

*Rashmi Panda* [*], *N.B. Puhan, Ganapati Panda*

*School of Electrical Sciences, Indian Institute of Technology Bhubaneswar, India*

ARTICLE INFO

ABSTRACT

Automated retinal vessel segmentation plays an important role in computer-aided diagnosis of serious diseases such as glaucoma and diabetic retinopathy. This paper contributes, (1) new Binary Hausdorff Symmetry (BHS) measure based automatic seed selection, and (2) new edge distance seeded region growing (EDSRG) algorithm for retinal vessel segmentation. The proposed BHS measure directly provides a binary symmetry decision at each pixel without the computation of continuous symmetry map and image thresholding. In a multiscale mask, the BHS measure is computed using the distance sets of opposite direction angle bins with sub-pixel resolution. The computation of the BHS measure from the Hausdorff distance sets involves point set matching based geometrical interpretation of symmetry. Then, we design a new edge distance seeded region growing (EDSRG) algorithm with the acquired seeds. The performance evaluation in terms of sensitivity, specificity and accuracy is done on the publicly available DRIVE, STARE and HRF databases. The proposed method is found to achieve state-of-the-art vessel segmentation accuracy in three retinal databases; DRIVE-sensitivity (0.7337), specificity (0.9752), accuracy (0.9539); STARE-sensitivity (0.8403), specificity (0.9547), accuracy (0.9424); and HRF-sensitivity (0.8159), specificity (0.9525), accuracy (0.9420).

© 2015 Nałęcz Institute of Biocybernetics and Biomedical Engineering. Published by Elsevier Sp. z o.o. All rights reserved.

## 1. Introduction

Retinal blood vessel morphology such as vessel diameter, branching, tortuosity, neovascularization, arteriovenous nicking provides important and valuable information about many serious disorders of eye and other physiological processes [1]. Image processing based removal of blood vessels in optic disc region enables better assessment of glaucoma [2]. Neovascularization is a sign of diabetic retinopathy [3]. Changes in vessel branching and tortuosity are symptoms of hypertensive retinopathy [4,5]. The presence of arteriovenous nicking is an important indicator of stroke [6]. Hence, the diagnostic information regarding these diseases is linked to accurate extraction of retinal blood vessels.

* *Corresponding author at*: School of Electrical Sciences, Indian Institute of Technology Bhubaneswar, India.
E-mail addresses: rp14@iitbbs.ac.in (R. Panda), nbpuhan@iitbbs.ac.in (N.B. Puhan), gpanda@iitbbs.ac.in (G. Panda).

When a large number of patients undergo regular screening, computer-aided diagnosis provides more effective solution instead of using only manual measurements. Further, automatic segmentation and analysis of retinal vasculature can improve reliability and reproducibility of decision making. Automated retinal vessel segmentation encounters several challenges: complex nonlinear structure of blood vessels, wide range of widths (scale), variable low contrast between blood vessels and background, various structures like optic disc, fovea and exudates interrupt the vessel segmentation process.

In literature, the supervised segmentation methods utilize ground truth images for the classification of vessels based on a given set of features. Niemeijer et al. [7] and Staal et al. [8] applied k-nearest neighbor (KNN) algorithm to estimate the probability of the pixel belonging to a vessel. Soares et al. [9] used a Bayesian classifier with class-conditional probability density functions (likelihoods) described as Gaussian mixtures. The feature vector is composed of pixel's intensity and response of the Gabor wavelet transform. Lupascu et al. introduced feature-based AdaBoost classifier for retinal blood vessel segmentation [10]. Ricci and Perfetti [11] employed line operators and support vector machine based classification. A five-layer feed-forward neural network is used by Marin et al. [12] and the feature vector is computed by combination of moment-invariant and gray-level features. Gardner et al. [13] proposed a back propagation multilayer neural network (NN) for vascular tree segmentation. The NN was fed with the values of the pixel in a $20 \times 20$ window at each pixel after histogram equalization, smoothing and edge detection.

The unsupervised methods work without any prior labeling knowledge. The concept of matched filter for retinal blood vessel extraction was proposed by Chaudhuri et al. [14]. The authors explored cross-sectional Gaussian intensity profile of blood vessel. Hoover et al. [15] and Gang et al. [16] further exploited this approach using a threshold probing technique to test whether the local piece is a vessel or not. Zhang et al. [17] used zero mean Gaussian filter and first order derivative of Gaussian (FODG) to detect the blood vessel.

Zana et al. [18] applied morphological filters in combination with cross-curvature evaluation to segment vessel-like patterns in retinal images. Mendonca et al. [19] used the Difference of Offset Gaussian (DoOG) filter to detect the centerline and then applied multiscale morphological reconstruction with iterative region growing to segment the blood vessel. Fraz et al. [20] detected the centerline and subsequently applied multidirectional morphological top-hat operator with a linear structuring element followed by bit plane slicing to detect the blood vessel. Odstrcilik et al. proposed a matched filtering based method in a newly created High Resolution Fundus (HRF) retinal database [21].

Chutatape et al. [22] used second order Gaussian matched filter to find the centerline points and then used Kalman filters and branch detection method for tracking blood vessels in retinal images. Can et al. [23] proposed a real time vessel tracking algorithm using directional templates around each candidate vessel point. Condurache et al. described a paradigm of hysteresis-classifier for vessel segmentation with multidimensional feature vector [24].

Frangi et al. [25] examined the multiscale second order (Hessian) local structure of MRA (angiogram) image in the context of developing a vessel enhancement filter. The vesselness measure is obtained on the basis of eigenvalue analysis of the Hessian matrix. Similar approach has been applied for retinal blood vessel segmentation by Martinez et al. in [27]. They applied first and second derivative (edge and maximal principal curvature) in multiple scales. In [28], a vesselness likelihood ratio is used for vessel centerline extraction that combines multiscale matched filter response, confidence measures and vessel boundary measures. In [29], multiscale line operator is investigated for segmentation of retinal blood vessel. Espona et al. [30] used the classical snake in combination with blood vessel topological properties to extract the vasculature from retinal images. Mahadevan et al. [31] used a variety of vessel profile models including Gaussian, derivatives of Gaussian and dual Gaussian and various noise models like Gaussian and Poisson noise. The gradient vector flow approach has been applied for retinal blood vessel segmentation by Tang et al. in [32]. A detailed survey on retinal blood vessel segmentation can be found in the paper by Kirbas et al. [33] and Fraz et al. [34].

In this paper, we follow a seeded region growing approach for accurate retinal vessel segmentation. The seeded region growing process starts from a set of selected seeds and grows into its neighbors being guided by regional features [35]. Automatic seed selection thus plays a critical role in seeded region growing based segmentation. In this paper, our contribution is twofold. First, we explore the symmetry property inherent in the blood vessel geometry to design a new Binary Hausdorff Symmetry (BHS) measure. The BHS measure enables accurate seed (centerline) selection in retinal blood vessels. Unlike the existing symmetry measure, the BHS measure does not require any continuous symmetry map and image thresholding computation. Secondly, the selected seed pixels are applied into the newly designed edge distance region growing (EDSRG) algorithm for vessel segmentation.

The rest of the paper is organized as follows: In Section 2, we present the new Binary Hausdorff Symmetry (BHS) measure followed by edge distance seeded region growing algorithm. Section 3 describes three publicly available retinal image databases along with the performance measures. The section also contains the results and comparison with existing methods. Finally, Section 4 concludes the paper.

## 2. Proposed vessel segmentation method

In this section, we propose a new Binary Hausdorff Symmetry (BHS) measure for automatic seed selection along with the EDSRG algorithm. The proposed vessel segmentation method can be divided into four parts; (1) image preprocessing, (2) identification of seed (centerline) pixels using the BHS measure, (3) postprocessing to remove false centerline pixels, (4) vessel segmentation using the new edge distance seeded region growing (EDSRG). A preliminary version of the proposed method can be found in [36]. Fig. 1(a) is considered as a test image for demonstration of the proposed method.
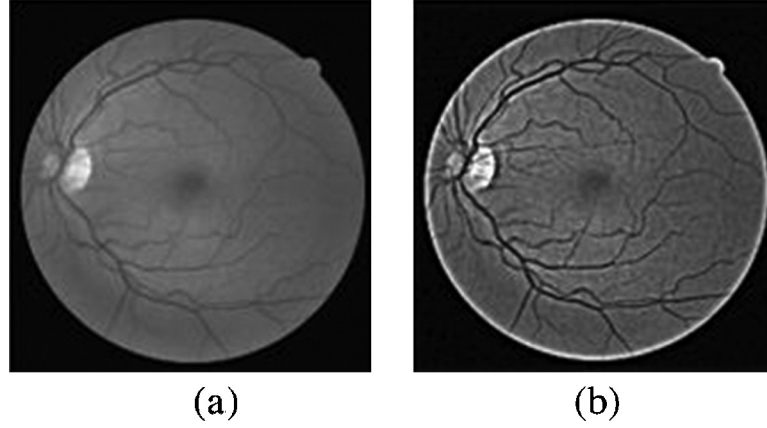
**Fig. 1 – (a) Retinal image (green channel) from the DRIVE database. (b) Retinal image after preprocessing.**

## 2.1. Image preprocessing

We consider the green channel of the RGB retinal (fundus) color image in our work since it is observed to contain better contrast between the vessels and background [7,11,18,19]. Further, image preprocessing is required as the intensity difference between the background and blood vessel is inadequate. There is gradual intensity variation from retinal periphery towards the central macular region. The intensity of the blood vessel is not constant throughout. Therefore, to achieve better contrast, we apply highboost filtering [37] to sharpen the input image before centerline detection. First, the image $f(x, y)$ is blurred using an arithmetic mean kernel ($\overline{f}(x, y)$) of size $21 \times 21$. The blurred image is subtracted from the original image to get the unsharp mask $g_{mask}(x, y)$. Finally, a weighted portion of the mask is added to the original image to get the sharpened image $g(x, y)$.

$$g_{mask}(x, y) = f(x, y) - \overline{f}(x, y) \tag{1}$$

$$g(x, y) = f(x, y) + k * g_{mask}(x, y) \tag{2}$$

The original green channel fundus image and the enhanced image are shown in Fig. 1.

## 2.2. BHS measure based centerline detection

The centerline pixel is observed to be symmetric with respect to the edges of the blood vessel. The distances from the candidate centerline pixel to edge pixels in opposite directions will thus be similar. Hence, we find the distance and orientation of each non-edge pixel to the edge pixels present in a pre-defined mask. The maximum width of the blood vessels outside optic disc area varies between 9 and 11 pixels. But inside the optic disc area, the blood vessels are thicker and the maximum width is approximately 15–17 pixels. As the width of the blood vessel varies within this range, we have considered the masks of multiple scales (9, 11, 13, 15, and 17).

### 2.2.1. Distance set generation

The edge image required in the method is obtained by applying the Canny edge operator [38,39]. To avoid the unwanted edges a threshold of 0.12 is considered, so that the edges which are not stronger than the threshold values are ignored. The candidate centerline pixels are determined at each scale and finally combined to get the seeds. Let the total number of edge pixels in the mask of a particular scale be $N_s$ ($s = 9$, 11, 13, 15, and 17). The distance $D_i$ and orientation $\theta_i$ of the edge pixel $E_i$ is computed from a non-edge pixel $P$ situated at the center of the mask (Fig. 2(a)). The proposed BHS measure decides if the pixel $P$ is a symmetric (centerline) pixel.

The orientation $\theta_i$ can vary from $0°$ to $360°$. We divide the whole orientation range into equal bins of $\alpha°$ interval. The total number of bins is $M$ which is equal to $(360/\alpha)$. After computing $D_i$ and $\theta_i$ for all edge pixels in the mask, we find the distance set $S_k$ containing the distance values $D_i$ falling into $k$th angle bin,

$$S_k = \{D_i | (k-1) \times \alpha° \leq \theta_i \leq k \times \alpha°\}, \quad k = 1, 2, \ldots, M. \tag{3}$$

If the mask center pixel is truly centerline, then the distance sets will be similar for opposite quadrant angle bins about the horizontal axis. So, the distance set in the $j$th angle bin ($S_j$) is compared with the corresponding distance set in the $(j + (m/2))$th angle bin ($S_{j+(M/2)}$). For example, $S_1$ is compared with $S_{37}$, $S_2$ with $S_{38}$ and so on, when the $M$ value becomes 72. Now, we formulate the similarity between the distance sets derived from opposite quadrant angle bins as the point set matching problem. Here, the Hausdorff distance measure [40] is considered as an effective technique for similarity computation with ($M/2$) pairs of distance (point) sets.

### 2.2.2. Hausdorff distance

The Hausdorff distance was originally designed as a dissimilarity measure defined on point sets. It was proposed by Huttenlocher et al. for object detection and recognition [40]. It later found wide application in image comparison [40,41]. The Hausdorff distance is defined in terms of distance between two point sets. Let $A = \{a_1, a_2, \ldots, a_m\}$ and $B = \{b_1, b_2, \ldots, b_m\}$ be two point sets. Then, the Hausdorff distance between sets $A$ and $B$ is given by

$$H(A, B) = \max(h(A, B), h(B, A)) \tag{4}$$

where $h$ is the directed Hausdorff given by

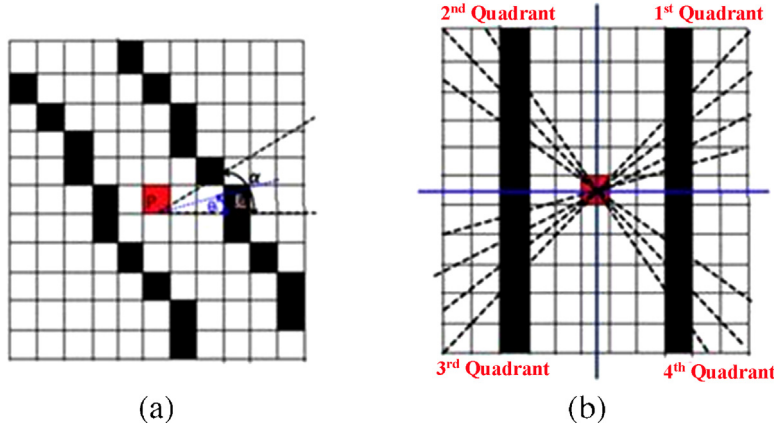$$h(A, B) = \max_{a_i \in A} \min_{b_i \in B} \|a_i - b_i\| \tag{5}$$

**Fig. 2 – (a) An example of 11 × 11 mask used for finding the Hausdorff distance values ($D_i$). (b) Quadrant concept interpretation.**

Here $h(A, B)$ and $h(B, A)$ are directed Hausdorff distances from $A$ to $B$ and from $B$ to $A$ respectively. $h(A, B)$ finds the point $a_i$ whose distance from its nearest point in set $B$ is maximum among all points in set $A$. The Hausdorff distance $H(A, B)$ is then the maximum of the directed distances.

### 2.2.3. BHS measure computation

We compute the Hausdorff distance only when both distance sets $S_j$ and $S_{j+(M/2)}$ as defined earlier are found to be non-empty. Hence, there will be a maximum of $M/2$ Hausdorff distance values for a particular center pixel, when all the distance set pairs are found to be non-empty. However, we practically obtain a less number of non-empty sets as there are few number of edge pixels in the window of a particular scale and no edge exists along the blood vessel direction.

The Hausdorff distance is a measure of dissimilarity between the distance (point) sets. Lower is the Hausdorff distance, more is the similarity between two distance sets. Therefore, we have taken a threshold ($t$) to decide similarity using the Hausdorff measure. To exploit the fact that a true centerline pixel is surrounded by edge pixels in all four quadrants, we put the following conditions: (1) at least $T_{in}$ number of Hausdorff distance values, which are below $t$, are found with respect to the angle bins (first quadrant: $(0 - 90)°$) and (third quadrant: $(181 - 270)°$), (2) Similar condition holds good for the Hausdorff distance values computed with respect to the angle bins (second quadrant: $(91 - 180)°$) and (fourth quadrant: $(271 - 360)°$). This is depicted in Fig. 2(b).

We define $H_j^P(S_j, S_{j+M/2})$ as the Hausdorff distance between two opposite angle bins with $j = 1, 2, \ldots, M/2$. As mentioned before, $H_j^P(S_j, S_{j+M/2})$ is computed only when both $S_j$ and $S_{j+M/2}$ are non-empty. In Eqs. (6) and (7), we define two sets which contain the Hausdorff distance values between opposite quadrants.

$$H_{set1}^P = \{H_j^P | H_j^P \leq t \text{ and } 1 \leq j \leq M/4\} \qquad (6)$$

$$H_{set2}^P = \{H_j^P | H_j^P \leq t \text{ and } ((M/4) + 1) \leq j \leq M/2\} \qquad (7)$$

The pixel $P$ is symmetric if the Binary Hausdorff Symmetry (BHS) measure in Eq. (8) takes a value of 1.

$$BHS(P) = \begin{cases} 1, & \text{if} \left(\left|H_{set1}^P\right| + \left|H_{set2}^P\right|\right) \geq T_{total} \\ & \&\& \\ & \min\left(\left|H_{set1}^P\right|, \left|H_{set2}^P\right|\right) \geq T_{in} \\ 0, & \text{otherwise} \end{cases} \qquad (8)$$

### 2.2.4. Example of BHS measure computation

The BHS measure computation for the example mask is given in Table 1. In our experiments, we have considered the bin angle to be $5°(\alpha)$. Hence, there are 72 angle bins ($M$) containing the distance sets ($S_k$, $k = 1, 2, \ldots, 72$) and at most 36 ($M/2$) Hausdorff distance values if both the angle bins in opposite direction are non-empty. For the mask in Fig. 2(a) at scale ($s = 11$), we obtain a total of eight Hausdorff distance values (1.0000, 0, 0, 1.0000, 0.9759, 1.4031, 2.2254, 0). The angle bins with opposite quadrant angle bins are found as non-empty in eight cases. A lower value of $T_{total}$ will result in false centerline pixel detection. High values of $T_{total}$ is not considered because many genuine centerline pixels are missed out. Based on this trade off, we have chosen the optimum value of $T_{total}$ to be 6. Using similar arguments for trade-off between false positive and true negative in detection, the value of $T_{in}$ is chosen as 2 and $t$ as 1.

### 2.2.5. Sub-pixel resolution

Where the number of pixels between two vessel edges is even, the centerline pixel fails to be detected. This is because no point is exactly equidistant to the edge pixels in any direction (Fig. 3(a)). To overcome this problem, we consider Hausdorff

**Table 1 – Example of BHS measure computation.**

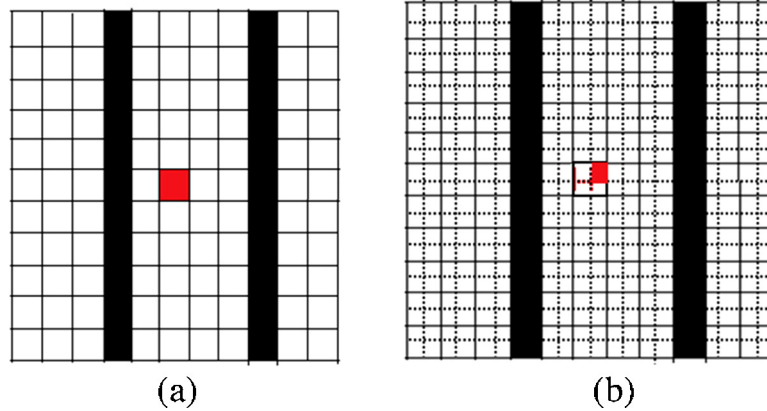| BHS computation | Values |
|---|---|
| $H_j^P(S_j, S_{j+M/2})$ | $H_1^P(S_1, S_{37}) = 1, H_6^P(S_6, S_{42}) = 0,$ $H_{13}^P(S_{13}, S_{49}) = 0, H_{19}^P(S_{19}, S_{55}) = 1,$ $H_{21}^P(S_{21}, S_{57}) = 0.9759, H_{29}^P(S_{29}, S_{65}) = 1.4031,$ $H_{30}^P(S_{30}, S_{66}) = 2.2254, H_{33}^P(S_{33}, S_{69}) = 0$ |
| $H_{set1}^P$ | $\{H_1^P, H_6^P, H_{13}^P\} = \{1, 0, 0\}$ |
| $H_{set2}^P$ | $\{H_{19}^P, H_{21}^P, H_{33}^P\} = \{1, 0.9759, 0\}$ |
| $BHS(P)$ | $\left|H_{set1}^P\right| = 3, \ \left|H_{set2}^P\right| = 3, \ \text{and} \ \left|H_{set1}^P\right| + \left|H_{set2}^P\right| = 6$ Thus, $BHS(P) = 1$ |

**Fig. 3 – (a) An example of 11 × 11 mask in unit pixel resolution (detected as non-centerline). (b) The mask in sub-pixel resolution (detected as centerline).**

measure in sub-pixel resolution (Fig. 3(b)). In sub-pixel resolution, a cell (pixel) in the image is virtually divided into $n$ sub-cells (sub-pixels). In our method, we have divided each cell into 4 sub-cells. Hence, there are extra horizontal and vertical grids at the middle of the cell, shown by the dotted lines in Fig. 3(b). Then, we compute the BHS measure for each sub-cell using Eqs. (3)–(8). If a sub-cell is detected as centerline, then the corresponding pixel in the unit resolution image is detected as centerline.

Finally, the centerline pixels obtained by using the multiscale masks in sub-pixel resolution are combined to obtain the seeds. The set of seed pixels obtained using the BHS measure with single scale ($s = 11$) and unit pixel resolution is shown in Fig. 4(a). Similarly, the final centerline image is shown with multiscale and sub-pixel resolution approach in Fig. 4(b). It is observed that the number of centerline pixels obtained by using multiscale masks in sub-pixel resolution is significantly increased.

### 2.2.6. Postprocessing

Among the detected pixels, the false centerline pixels are detected between two closely placed blood vessels. To remove such cases, we apply $k$-means clustering [42] and the support vector machine (SVM) [43] on the detected centerline pixels. In both the cases, the feature vector is $3 \times 3$ pixel intensity neighborhood of the centerline pixel along with the mean. Hence, the feature vector size is 10 for each centerline pixel.

For clustering, we initialize two centroids as the pixels with minimum and maximum mean value of $3 \times 3$ pixel neighborhood among all the centerline pixels. For SVM, we took any one ground truth image from the database for training purpose. Then the centerline image obtained by using BHS measure is superimposed on the ground truth image. The pixels of the centerline image lying inside the ground truth blood vessels are considered as true centerline pixels and rest are defined as false centerline pixels. The feature vector of these pixels for training purpose is same as the feature vector taken for $k$-means clustering. The true centerline pixels after removing false centerline cases using $k$-means clustering and SVM are shown in Fig. 4(c) and (d), respectively. SVM is a supervised technique where as clustering is an unsupervised technique. Both methods are separately applied to convey that any supervised/unsupervised method can be used to remove the false centerlines.

We quantify the performance of the proposed postprocessing step using the ground truth and produced centerline images in DRIVE, STARE and HRF databases. The performance measures, BRR (Background Rejection Ratio) and CRR (Centerline Retention Ratio) are given as:

$$BRR = \frac{N_B - N_B^P}{N_B} \times 100 \qquad (9)$$

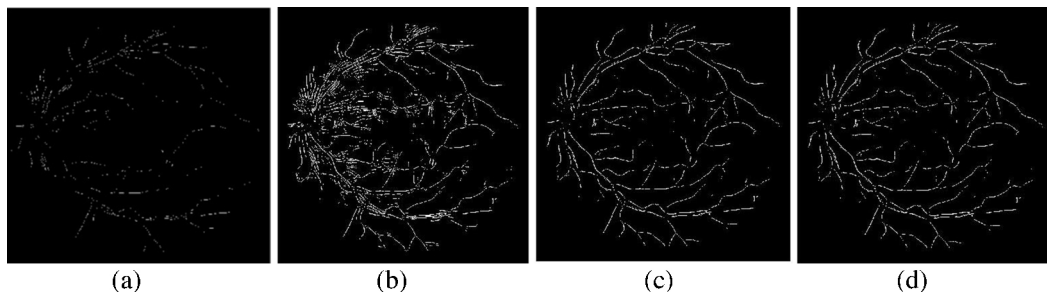$$CRR = \frac{N_{center}^P}{N_{center}} \times 100 \qquad (10)$$



**Fig. 4 – (a) Vessel centerlines detected with single scale ($s = 11$) in unit pixel resolution. (b) Vessel centerlines detected with multiscale sub-pixel resolution. True centerline pixels: (c) after $k$-means clustering (d) after SVM postprocessing.**

where $N_B$ and $N_B^P$ (number of background pixels), $N_{center}$ and $N_{center}^P$ (number of centerline pixels) are detected before and after postprocessing, respectively. In Table 2, the performance measures of the postprocessing are shown to achieve high values to retain true centerline pixels and remove false background pixels.

## 2.3. Edge distance seeded region growing (EDSRG) algorithm

Seeded region growing performs segmentation in an image with respect to an initial set of points, known as seeds [35,44]. The region growing method starts with one or more seeds and fills the regions starting from the seed points. The neighboring pixels are visited in a specific order and depending on the fulfillment of a similarity criterion (also known as aggregation criteria), they can be added to the region [44,45]. We propose an edge distance seeded region growing (EDSRG) algorithm which achieves effective retinal segmentation performance. We grow the region from the selected seeds till we reach the edges. For doing so, we satisfy certain geometry based constraints. The output image of the proposed centerline detection technique serves as the input to EDSRG algorithm. There is no other interaction between the BHS and EDSRG algorithm in terms of parameters.

Centered at every seed pixel, we consider $W \times W$ window in the edge image. Then, we scan each pixel present in the window. In the window, there might be more than one seed pixels and many edge pixels. For each non-edge and non-seed pixel $P$ in the window, we find the nearest seed pixel $S_n$ and nearest edge pixel $E_n$ in Fig. 5(a). The distance from the pixel $P$ to the nearest seed ($D_{PS_n}$) and the distance between the nearest seed to nearest edge ($D_{S_nE_n}$) is computed. The pixel $P$ is a candidate vessel pixel if $D_{PS_n}$ is found to be less than $D_{S_nE_n}$.

For pixels outside the blood vessel, the distance $D_{PS_n}$ is always greater than $D_{S_nE_n}$. Hence the background pixel will not be classified as blood vessel in case of broken boundary case; thus leakage is avoided. The above mentioned condition fails if there are multiple edges lines present around the seed in the window (Fig. 5(b)). To solve this particular difficulty, we suggest an additional constraint, i.e. there should not be any edge pixel on the line ($L$) joining the nearest seed point and nearest edge point. The EDSRG algorithm is formulated in the following:

**EDSRG Algorithm**
Input: Set of seed pixels, edge input image
Output: Segmented blood vessel image
For a window of size $W \times W$ centered on every seed pixel
For every non-edge and non-seed pixel $P$ in the window
Find
$D_{PS_n}$: Distance of $P$ to the nearest seed pixel $S_n$
$D_{S_nE_n}$: Distance of $S_n$ to the nearest edge pixel $E_n$
$L$: Line joining the pixels $S_n$ and $E_n$
The pixel $P$ is included in the segmented output, if
$D_{S_nE_n} \geq D_{PS_n}$ and there is no edge pixel situated on the line $L$.

The final segmentation output after applying the proposed EDSRG algorithm is shown in Fig. 6. The parameter $W$ is experimentally chosen as 11 for obtaining high performance. Retinal vessel segmentation output for various test images from the DRIVE, STARE and HRF databases are shown in Fig. 7.

## 3. Results and discussion

### 3.1. Retinal image databases

In literature, retinal blood vessel segmentation algorithms are evaluated using publicly available standard databases (DRIVE

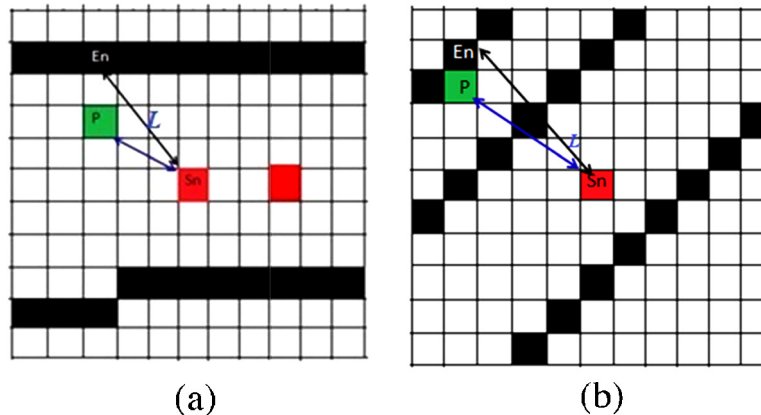| Table 2 – Performance measures of the postprocessing. | | | | | | |
|---|---|---|---|---|---|---|
| Performance measures | DRIVE | | STARE | | HRF | |
| | Clustering | SVM | Clustering | SVM | Clustering | SVM |
| BRR | 89.37 | 88.37 | 91.88 | 91.37 | 89.51 | 89.10 |
| CRR | 92.84 | 91.72 | 91.56 | 90.93 | 92.52 | 92.04 |



Fig. 5 – (a) Region growing with a true centerline case. (b) Region growing with multiple edges in the mask.
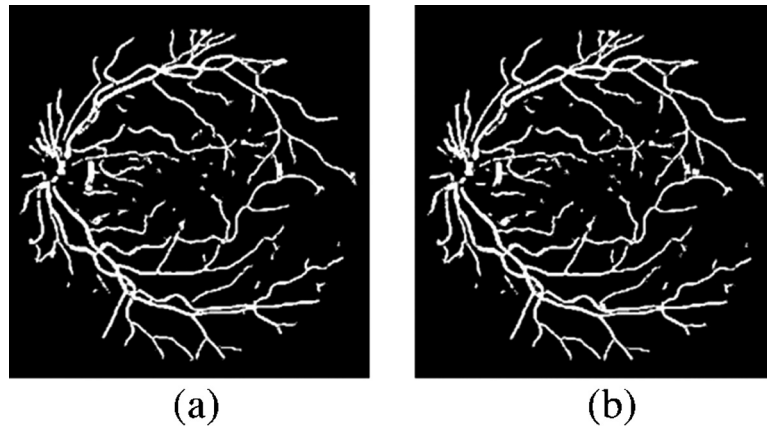
**Fig. 6 – Blood vessel segmentation: (a) Using seeds after *k*-means clustering; (b) Using seeds after SVM postprocessing.**
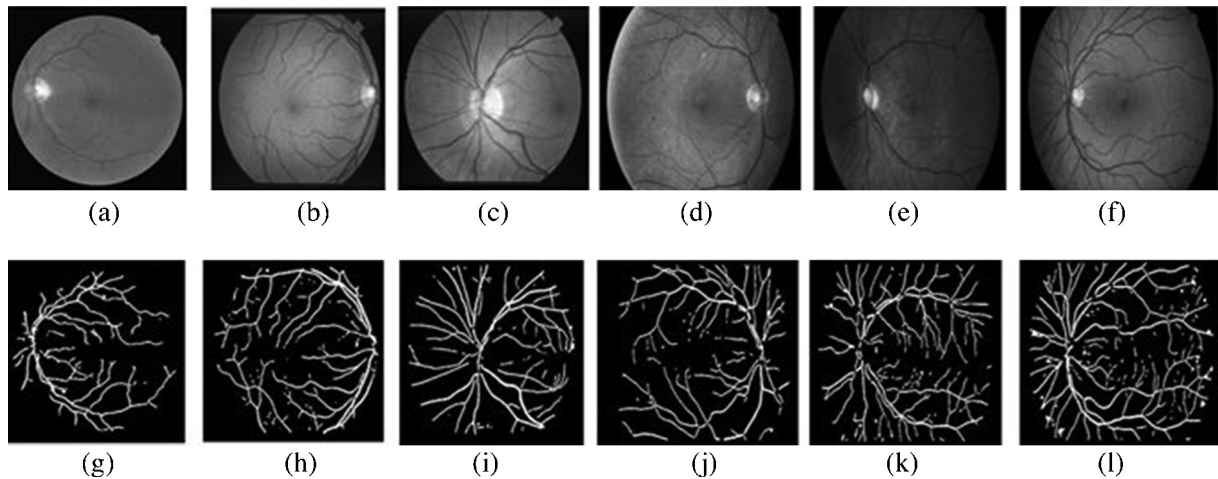


**Fig. 7 – Retinal images: (a) DRIVE; (b, c) STARE; (d) HRF diabetic retinopathy; (e) HRF glaucomatous; (f) HRF healthy image; (g–l) Corresponding retinal blood vessel segmentation outputs.**

[46] and STARE [15]). For each image, two manually segmented blood vessel images generated by two different specialists are available. The segmented images by the first observer are used as ground truth for performance evaluation.

The DRIVE (Digital Retinal Images for Vessel Extraction) database contains 40 color retinal (fundus) images. The photographs were obtained from a diabetic retinopathy screening program in the Netherlands. The database is divided into test and training sets. Each of the sets contains 20 images. Seven images of the database contain pathological symptoms. The images are captured with a Canon CR5 non-mydriatic 3-CCD camera with a 45° field-of-view (FOV). Each image is digitized to 768 × 584 pixels and 8 bits per color plane. The images are provided in TIFF format. The database also provides corresponding FOV masks, which are circular in shape. The STARE (STructured Analysis of REtina) database comprises of 20 color fundus images (ten of which contains pathology). The images are taken with a TopCon TRV-50 fundus camera at 35° FOV. Each image has 700 × 605 pixels and 8 bits per color plane. The images in the database are in the PPM format.

Recently, a new HRF database is publicly available for performance evaluation of retinal vessel segmentation [21]. The HRF (High Resolution Fundus image) database contains three sets of fundus images with healthy retinas, retinas affected by glaucoma and diabetic retinopathy. Each set is composed of 15 images. The images are acquired with a CANON CF-60 UVi equipped with CANON EOS-20D digital fundus camera with a 60° FOV. Each image size is 3504 × 2336 pixels and 8 bits per color plane. The images are stored in the JPEG format. For each image, a binary mask determining the FOV and human segmented blood vessel ground truth is provided.

### 3.2. Performance measures

In retinal blood vessel segmentation, there are only two possibilities for a pixel i.e. to be either in blood vessel or in the background. The number of pixels correctly classified as vessel pixels is true positive (TP) and vessel pixels incorrectly classified as background is called as false negative (FN). Similarly, the number of pixels correctly classified as background is true negative (TN) and background pixels incorrectly

**Table 3 – Performance measures of the vessel segmentation methods (DRIVE).**

| Method | | SN | SP | ACC |
|---|---|---|---|---|
| 2nd Human Observer | | 0.7736 | 0.9725 | 0.9470 |
| Lupascu et al. [10] | | N.A. | N.A. | 0.9597 |
| Zana et al. [18] | | 0.6971 | N.A. | 0.9377 |
| Martinez et al. [26] | | 0.6389 | N.A. | 0.9551 |
| Chaudhuri et al. [14] | | N.A. | N.A. | 0.8733 |
| Mendonca et al. [19] | | 0.7344 | 0.9764 | 0.9452 |
| Sores et al. [9] | | 0.7285 | 0.9786 | 0.9466 |
| Staal et al. [8] | | 0.7345 | N.A. | 0.9442 |
| Ricci et al. [11] | | N.A. | N.A. | 0.9563 |
| Fraz et al. [20] | | 0.7152 | 0.9769 | 0.9430 |
| Niemeijer et al. [7] | | N.A. | N.A. | 0.9416 |
| Martinez et al. [27] | | 0.7246 | 0.9655 | 0.9344 |
| Tang et al. [32] | | N.A. | N.A. | 0.9106 |
| Proposed BHS centerline + EDSRG (Type I) | Clustering | 0.7038 | 0.9582 | 0.9353 |
| | SVM | 0.7146 | 0.9434 | 0.9229 |
| Proposed BHS centerline + region growing [19] (Type II) | Clustering | 0.7328 | 0.9752 | 0.9539 |
| | SVM | 0.7337 | 0.9738 | 0.9527 |

**Table 4 – Performance measures of the vessel segmentation methods (STARE).**

| Method | | SN | SP | ACC |
|---|---|---|---|---|
| 2nd Human Observer | | 0.8951 | 0.9565 | 0.9348 |
| Hoover et al. [15] | | 0.6751 | 0.9567 | 0.9267 |
| Staal et al. [8] | | 0.6970 | 0,9810 | 0.9516 |
| Sores et al. [9] | | 0.7197 | 0.9747 | 0.9478 |
| Mendonca et al. [19] | | 0.6996 | 0.9730 | 0.9440 |
| Fraz et al. [20] | | 0.7311 | 0.9680 | 0.9442 |
| Ricci et al. [11] | | N.A. | N.A. | 0.9584 |
| Martinez et al. [27] | | 0.7506 | 0.9569 | 0.9410 |
| Proposed BHS centerline + EDSRG (Type I) | Clustering | 0.7385 | 0.9547 | 0.9368 |
| | SVM | 0.7446 | 0.9470 | 0.9395 |
| Proposed BHS centerline + region growing [19] (Type II) | Clustering | 0.8403 | 0.9504 | 0.9424 |
| | SVM | 0.8390 | 0.9507 | 0.9417 |

$$ACC = \frac{TP + TN}{TP + FN + TN + FP} \tag{13}$$

classified as blood vessel is called false positive (FP). The performance is evaluated in terms of sensitivity (SN), specificity (SP), and accuracy (ACC) measures. Sensitivity (SN) reflects the ability of an algorithm to detect the vessel pixels. Specificity (SP) is the ability to detect non-vessel pixels. The accuracy (ACC) is measured by the ratio of the total number of correctly classified pixels to the number of pixels in the image.

$$SN = \frac{TP}{TP + FN} \tag{11}$$

$$SP = \frac{TN}{TN + FP} \tag{12}$$

## 4. Discussion

The proposed BHS measure based seed selection along with EDSRG method is implemented on DRIVE, STARE and HRF databases. The performance measures are computed on each database image with respect to the ground truth. The proposed method, being an unsupervised method, does not need (manually) labeled training data. Tables 3–5 demonstrate that it has been possible to design a new system that achieves the state-of-the-art performance. From the tables, we observe that the proposed method's high segmentation performance (Type I) is comparable and better than the existing methods in DRIVE, STARE and HRF databases.

**Table 5 – Performance measures of the vessel segmentation methods (HRF).**

| Method | | | SN | SP | ACC |
|---|---|---|---|---|---|
| Odstrcilic et al. [21] | | Diabetic retinopathy | 0.7463 | 0.9619 | 0.9445 |
| | | Galucomatic | 0.7900 | 0.9638 | 0.9497 |
| | | Healthy | 0.7861 | 0.9750 | 0.9539 |
| | | Average | 0.7741 | 0.9669 | 0.9493 |
| Proposed BHS centerline + EDSRG (Type I) | Clustering | Diabetic retinopathy | 0.6662 | 0.9409 | 0.9219 |
| | | Galucomatic | 0.6658 | 0.9509 | 0.9311 |
| | | Healthy | 0.6846 | 0.9485 | 0.9239 |
| | | Average | 0.6722 | 0.9468 | 0.9256 |
| | SVM | Diabetic retinopathy | 0.6919 | 0.9221 | 0.9061 |
| | | Galucomatic | 0.7165 | 0.9429 | 0.9275 |
| | | Healthy | 0.7325 | 0.9375 | 0.9185 |
| | | Average | 0.7103 | 0.9342 | 0.9174 |
| Proposed BHS centerline + region growing [19] (Type II) | Clustering | Diabetic retinopathy | 0.7883 | 0.9471 | 0.9362 |
| | | Galucomatic | 0.8219 | 0.9484 | 0.9399 |
| | | Healthy | 0.8325 | 0.9619 | 0.9499 |
| | | Average | 0.8142 | 0.9525 | 0.9420 |
| | SVM | Diabetic retinopathy | 0.7882 | 0.9446 | 0.9338 |
| | | Galucomatic | 0.8248 | 0.9475 | 0.9393 |
| | | Healthy | 0.8347 | 0.9604 | 0.9490 |
| | | Average | 0.8159 | 0.9508 | 0.9407 |
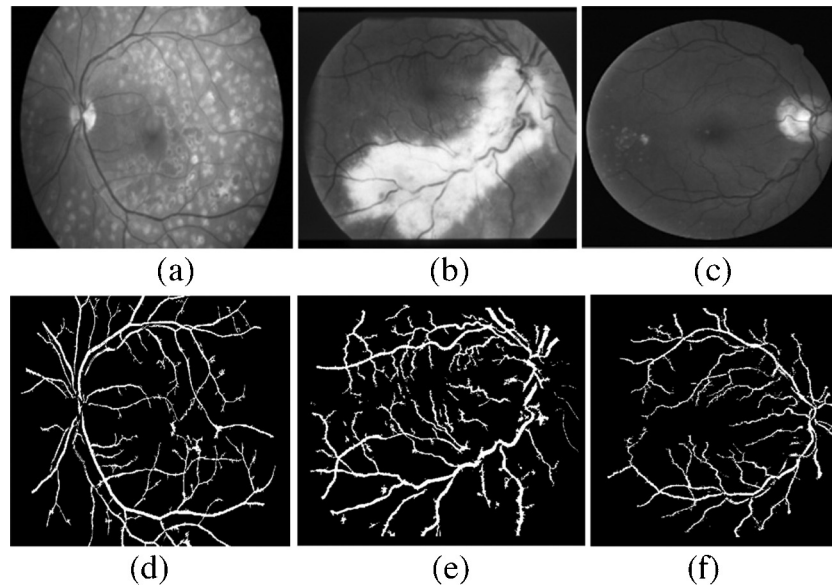
Fig. 8 – (a–c) Green channel images of pathological retina. (d–f) Retinal blood vessel segmentation results.

To check the robustness of the BHS measure based seed selection, we combined it with the region growing of [19]. We named the hybrid method (BHS measure based seed selection method along with region growing technique of [19]) as Type II method. The region growing technique used by [19] is based on morphological reconstruction. Morphological reconstruction is an image transformation that requires two images: one marker image which acts as the starting point for the transformation and the other image is the mask which constrains the transformation. In [19] double thresholding is done with the narrow (for marker image) and wide (for mask image) range of threshold values on enhanced gray scale images at multiple scales. Later on a multiple iteration vessel filling (region growing) procedure is applied to get the blood vessels. In the first iteration the centerline pixels are used as seeds which breed upon the reconstructed image of smallest scale. In rest iterations, the reconstructed image at higher scale is used to extend the output of previous region growing step.

This Type II method results higher sensitivity values with comparable specificity and accuracy values. This means the proposed seed selection methodology segments the blood vessels more accurately than the existing method. In STARE and HRF database containing pathological images, the proposed Type I and Type II method provide a significant increase in the sensitivity measure with high specificity and accuracy performance.

The proposed algorithm is not affected by the edges of bright or dark spots in pathological images. The proposed BHS measure is a local symmetry measure, which detects the symmetric points in masks of size slightly more than the vessel width. Hence, seed points are not selected when pathologies are encountered. In case of smaller spots less than the width of blood vessel, the detected symmetric points are removed in the post processing step. As we consider multi scale masks, we obtain robust symmetric point detection in

the presence of vessels with different size. Thus it generates correct segmentation of blood vessels even in case of pathological images as shown in Fig. 8.

The symmetry measure has been an effective tool for object detection and tracking in natural images. Hence, we consider the popular generalized symmetry transform (GST) [47] to detect the symmetric centerline pixels for performance evaluation with respect to retinal vessel segmentation. We implement GST in multiple scales to detect the points of symmetry inside the blood vessels. The method is found to assign such pixels with high values of continuous symmetry measure. Then, we obtain the symmetric pixels from the continuous symmetry map through automatic image thresholding for each scale [48]. The obtained centerline pixels are used as seeds in the EDSRG algorithm. The average performance measures of GST on three publicly available databases are given in Table 6. The performance quantified on the basis of sensitivity measure is due to the less number of detected centerline pixels.

The threshold values used for computing the BHS measure in Eq. (8) are based on local vessel geometry. The experimental choice of $t$, $T_{total}$ and $T_{in}$ is consistent for every image and scale in DRIVE, STARE and HRF databases. The proposed BHS measure is different from the existing symmetry measure with respect to computing the symmetry decision. Other symmetry measures such as GST compare the continuous symmetry values among all pixels in the image thresholding step. On the

| Table 6 – Performance measures of GST. | | | |
|---|---|---|---|
| Database | Sensitivity (SN) | Specificity (SP) | Accuracy (ACC) |
| DRIVE | 0.4427 | 0.9827 | 0.9357 |
| STARE | 0.5285 | 0.9740 | 0.9409 |
| HRF | 0.5846 | 0.9545 | 0.9277 |

other hand, the BHS measure tests whether sufficient conditions of symmetry for a pixel are satisfied. Thus, the proposed BHS measure becomes binary and is found to be useful for seed selection in retinal images from multiple databases.

The second part of our proposed algorithm i.e. EDSRG method is simpler. It is based on the distance of the non-edge pixel to the seed point and nearest edge pixel. After the seed selection process, the only requirement for EDSRG method is the edge image which is obtained by canny edge operator. The broken edges are also taken care by our algorithms in such a way that there could not be any leakage. Hence our method avoids the complex procedure of threshold selection, mask and marker image generation, and multistage region growing operation as in [19]. Thus, the proposed edge distance based seeded region growing (EDSRG) is simple in implementation.

The EDSRG algorithm is leak proof and results in accurate segmentation in the presence of broken and multiple edges. Our approach for blood vessel segmentation is robust as far as variation in the background and central reflexes are concerned. However, in case of thin blood vessels, variation in the image intensity between vessel and background are the least. Hence, the edges are sometimes not detected. As our region growing method is edge dependant, the finest blood vessels are sometimes missed due to absence of edges. That is why the accuracy of Type II method is slightly higher than the Type I method. Our future work is focused towards the improvement of segmentation results in the optic disc and thin blood vessel region. On a desktop computer with Intel Core i7, 3.4 GHz CPU and 8 GB RAM, it takes approximately 4.1 min on an average to segment the blood vessels using our proposed method. To achieve higher computational performance in future work, different programming environment and parallel image processing can be considered for implementation of the method.

## 5.     Conclusion

In this paper, we explored the symmetry nature of the centerline pixels with reference to blood vessel boundaries. We first proposed a novel Binary Hausdorff Symmetry (BHS) measure based seed selection technique. The BHS measure along with multiscale masks and sub-pixel resolution accurately detects a significant number of seed pixels. The EDSRG (Type I) and morphological reconstruction based region growing (Type II) are applied with the acquired seeds to segment blood vessels. The newly proposed method is validated on three publicly available databases (DRIVE, STARE and HRF) and found to achieve high performance comparable and better with state-of-the-art methods. The superior performance of the proposed method (Type-II) as compared to (Type-I) indicates further scope to improve the region growing algorithm in future work.

## REFERENCES

[1] Bowling B. Clinical ophthalmology. 6th ed. London, UK: Elsevier Health Sciences; 2012.

[2] Meier J, Nyúl LG, Hornegger J, Michelson G. Glaucoma risk index: automated glaucoma detection from color fundus images. Med Image Anal 2010;14(3):471–81.

[3] Rajan SE. Computerized screening of diabetic retinopathy employing blood vessel segmentation in retinal images. Biocybern Biomed Eng 2014;34(2):117–24.

[4] Flynn J, O'Keefe M, Cahill M. Characterization of changes in blood vessel width and tortuosity in retinopathy of prematurity using image analysis. Med Image Anal 2002;6 (4):407–29.

[5] Grisan E, Ruggeri A. Extraction and quantitative description of vessel features in hypertensive retinopathy fundus images. Book Abstracts 2nd International Workshop on Computer Assisted Fundus Image Analysis; 2001.

[6] Hunter A, Steel D, Basu A, Ryder R, Kennedy RL. Measurement of retinal vessel widths from fundus images based on 2-D modelling. IEEE Trans Med Imaging 2004;23 (10):1196–204.

[7] Staal J, Ginneken B, Loog M, Abramoff MD. Comparative study of retinal vessel segmentation methods on a new publicly available database. Proc. of SPIE Medical Imaging, vol. 5370. 2004. pp. 648–65.

[8] Abramoff MD, Niemeijer M, Viergever MA, Ginneken B. Ridge-based vessel segmentation in color images of the retina. IEEE Trans Med Imaging 2004;23(4):501–9.

[9] Leandro JJG, Cesar RM, Jelinek HF, Cree MJ. Retinal vessel segmentation using the 2-D Gabor wavelet and supervised classification. IEEE Trans Med Imaging 2006;25(9):1214–22.

[10] Tegolo D, Trucco E. FABC: retinal vessel segmentation using AdaBoost. IEEE Trans Inf Technol Biomed 2010;14 (5):1267–74.

[11] Perfetti R. Retinal blood vessel segmentation using line operators and support vector classification. IEEE Trans Med Imaging 2007;26(10):1357–60.

[12] Marin D, Aquino A, Gegundez-Arias ME, Bravo JM. A new supervised method for blood vessel segmentation in retinal images by using gray-level and moment invariants-based features. IEEE Trans Med Imaging 2011;30(1):146–58.

[13] Keating D, Williamson TH, Elliott AT. Automatic detection of diabetic retinopathy using an artificial neural network: a screening tool. Br J Ophthalmol 1996;80:940–4.

[14] Chatterjee S, Katz N, Nelson M, Goldbaum M. Detection of blood vessels in retinal images using two-dimensional matched filters. IEEE Trans Med Imaging 1989;8(3):263–9.

[15] Kouznetsova V, Goldbaum M. Locating blood vessels in retinal images by piecewise threshold probing of a matched filter response. IEEE Trans Med Imaging 2000;19(3):203–10.

[16] Chutatape O, Krishnan SM. Detection and measurement of retinal vessels in fundus images using amplitude modified second-order Gaussian filter. IEEE Trans Biomed Eng 2002;49(2):168–72.

[17] Zhang L, Zhang L, Karray F. Retinal vessel extraction by matched filter with first-order derivative of Gaussian. Comput Biol Med 2010;40(4):438–45.

[18] Klein JC. Segmentation of vessel-like patterns using mathematical morphology and curvature evaluation. IEEE Trans Image Process 2001;10(7):1010–9.

[19] Campilho A. Segmentation of retinal blood vessels by combining the detection of centerlines and morphological reconstruction. IEEE Trans Med Imaging 2006;25(9):1200–13.

[20] Barman SA, Remagnino P, Hoppe A, Basit A, Uyyanonvara B, Rudnicka AR, et al. An approach to localize the retinal blood vessels using bit planes and centerline detection. Comput Methods Programs Biomed 2012;108(2):600–16.

[21] Kolar R, Budai A, Hornegger J, Jan J, Gazarek J, Kubena T, et al. Retinal vessel segmentation by improved matched filtering: evaluation on a new high-resolution fundus image database. IET Image Process 2013;7(4):373–83.

[22] Zheng L, Krishnan SM. Retinal blood vessel detection and tracking by matched Gaussian and Kalman filters. Proc. IEEE Int. Conf. on Engineering in Medicine and Biology Society, vol. 6. 1998. pp. 3144–9.

[23] Hong S, Turner JN, Tanenbaum HL, Roysam B. Rapid automated tracing and feature extraction from retinal fundus images using direct exploratory algorithms. IEEE Trans Inf Technol Biomed 1999;3(2):125–38.

[24] Mertins A. Segmentation of retinal vessels with a hysteresis binary-classification paradigm. Comput Med Imaging Graphics 2012;36(4):325–35.

[25] Niessen WJ, Vincken KL, Viergever MA. Multiscale vessel enhancement filtering. Medical Image Computing and Computer-Assisted Intervention—MICCAI'98. Springer Berlin Heidelberg; 1998. p. 130–7.

[26] Hughes AD, Stanton AV, Thom SA, Bharath AA, Parker KH. Retinal blood vessel segmentation by means of scale-space analysis and region growing. Proc. Int. Conf. Medical Image Computing and Computer-Assisted Intervention. UK: Springer-Verlag; 1999. p. 90–7.

[27] Hughes AD, Thom SA, Bharath AA, Parker KH. Segmentation of blood vessels from red-free and fluorescein retinal images. Med Image Anal 2007;11:47–61.

[28] Stewart CV. Retinal vessel centerline extraction using multiscale matched filters, confidence and edge measures. IEEE Trans Med Imaging 2006;25(12):1531–46.

[29] Hatfield FN, Knox P, Reakes M, Spencer S, Parry D, Harding SP. Enhancement of blood vessels in digital fundus photographs via the application of multiscale line operators. J Franklin Inst 2008;345(7):748–65.

[30] Carreira MJ, Ortega M, Penedo MG. A snake for retinal vessel segmentation. Pattern Recognit Image Anal 2007;4478:178–85.

[31] Narasimha-Iyer H, Roysam B, Tanenbaum HL. Robust model-based vasculature detection in noisy biomedical images. IEEE Trans Inf Technol Biomed 2004;8:360–76.

[32] Ping Z. Segmentation of retinal blood vessel by merging shape, region and edge information. Proceedings of International Conference of Biomedical Engineering and Biotechnology (ICBEB); 2012. p. 888–91.

[33] Quek F. A review of vessel extraction techniques and algorithms. ACM Comput Surv – CSUR 2004;36(2):81–121.

[34] Remagnino P, Hoppe A, Uyyanonvara B, Rudnicka AR, Owen CG, Barman SA. Blood vessel segmentation methodologies in retinal images – a survey. Comput Methods Programs Biomed 2012;108(1):407–33.

[35] Bischof L. Seeded region growing. IEEE Trans PAMI 1994;16(6):641–7.

[36] Puhan NB, Panda G. Hausdorff symmetry operator towards retinal blood vessel segmentation. Proc. IEEE International Conference on Digital Signal Processing (DSP); 2014. pp. 611–6.

[37] Woods RE. Digital image processing. 3rd ed. Pearson Education India; 2004.

[38] A computational approach to edge detection. IEEE Trans PAMI 1986;8(6):679–98.

[39] Hlavac V, Boyle R. Digital image processing and computer vision. 2nd ed. USA: Cengage Learning; 2008.

[40] Klanderman GA, Rucklidge WA. Comparing images using the Hausdorff distance. IEEE Trans PAMI 1993;15(9):850–63.

[41] Puhan NB, Xia H, Jiang X. Iris recognition on edge maps. IET Comput Vis 2009;3(1):1–7.

[42] Narasimha Murty M, Flynn PJ. Data clustering: a review. ACM Comput Surv 1999;31(3):264–323.

[43] Vandewalle J. Least squares support vector machine classifiers. Neural Process Lett 1999;9(3):293–300.

[44] Zeng G, Body M, Hacid M. Seeded region growing: an extensive and comparative study. Pattern Recognit Lett 2005;26(8):1139–56.

[45] Yau DKY, Elmagarmid AK, Aref WG. Automatic image segmentation by integrating color-edge extraction and seeded region growing. IEEE Trans Image Process 2001;10 (10):1454–66.

[46] Niemeijer M, Staal JJ, Ginneken BV, Loog M, Abramoff MD. DRIVE: digital retinal images for vessel extraction; 2004, http://www.isi.uu.nl/Research/Databases/DRIVE.

[47] Wolfson H, Yeshurun Y. Context-free attentional operators: the generalized symmetry transform. Int J Comput Vis 1995;14(2):119–30.

[48] A threshold selection method from gray-level histograms. IEEE Trans Syst Man Cybern 1979;9(1):62–6.